UNCONVENTIONAL RESOURCES TECHNOLOGY CONFERENCE
FUELED BY SPE • AAPG • SEG

URTeC 1575434

The Evolution of Stimulated Reservoir Volume during Hydraulic Stimulation of Shale Gas Formations

Madhur Johri[1,2], Mark D. Zoback[1]
[1] Department of Geophysics, Stanford University, Stanford - CA
[2] Now at Upstream Technology, BP America, Houston – TX

This paper was prepared for presentation at the Unconventional Resources Technology Conference held in Denver, Colorado, USA, 12-14 August 2013.

1. Abstract

Flow rates in extremely low permeability shale gas reservoirs depend on the total area of permeable fractures that are hydraulically connected to the well and the matrix permeability of the shale formation. We study how co-seismic slip induced on pre-existing natural fractures and faults during hydraulic stimulation evolves the cumulative area of fractures contributing to flow. The study area is the Barnett gas field. We base our modeling on field data obtained during multistage hydraulic fracturing. We assume that only the propped hydraulic fractures and pre-existing fractures and faults that are stimulated in shear, are hydraulically conductive and contribute to flow. Thus, stimulation not only creates hydraulic fractures but also induces slip on a network of pre-existing fractures and faults, leading to a significant increase in the hydraulically active percolation zone responsible for production. We model slip on these pre-existing faults using two-dimensional plane-strain dynamic rupture models featuring a strongly rate-weakening friction and off-fault Drucker-Prager plasticity. Modeling predicts the formation of strain localization features (indicative of new fractures) at the tips of poorly oriented faults. The new fractures increase the percolation zone (and hence flow rate) by providing a larger cumulative area of fractures hydraulically connected to the well (larger area for gas to diffuse out of the formation) and by increasing the connectivity of the pre-existing fracture network (more reservoir penetration). This study, therefore, suggests three primary contributors to the increase in the percolation zone – the hydraulic fractures themselves, the pre-existing percolating fractures stimulated in shear, and the newly-formed and newly-connected percolating fractures. As the contribution from the hydraulic fractures is relatively small in the very low permeability Barnett (~100 nd) the magnitude of increase in the percolation zone and hence the amount of stimulation is directly correlated to the initial fracture population and is extremely important in controlling flow.

2. Introduction

Multi-stage slick-water hydraulic fracturing is a commonly deployed technology for stimulating organic-rich shale gas reservoirs in order to produce commercial quantities of natural gas. However, the physical mechanisms responsible for stimulating the formation are poorly understood. The common understanding is that water diffuses from the hydraulic fractures created during stimulation into the surrounding natural fractures and faults, and elevates pore pressure. Increase in pore pressure on the surface of these fractures reduces the effective normal stress on the fractures and induces shear slip. Much, but not all, slip events induced on fractures are expressed in the form of microseismicity (Zoback et al, 2012). The outstanding question, however, is how the formation of hydraulic fractures and co-seismic slip on pre-existing fractures and faults stimulates the formation in a manner that facilitates a dramatic increase in flow rates observed post stimulation.

In this study, we first discuss how slip on natural fractures and faults enhances fracture permeability. Second, we discuss the effect of co-seismic slip across pre-existing natural fractures and faults on the surrounding rock matrix. The matrix permeability (~100 nd) is too low to contribute to flow significantly, and is not expected to change much

during reservoir stimulation (as shown in section 4). Natural fractures contribute to flow only if they are hydraulically permeable and hydraulically connected to the well via hydraulically conductive flow paths including a hydraulically conductive fracture network and the hydraulic fractures. The total surface area of this interconnected network of fractures comprises the percolation zone. Gas diffuses out of the rock matrix into the fractures and flows along the fractures in the percolation zone towards the well. The percolation zone, therefore, represents the area within the reservoir that contributes to fluid flow. With this in mind, we finally investigate the impact of co-seismic slip across natural fractures and faults on the evolution of the percolation zone. This problem is studied in the framework of discrete fracture networks (DFNs) since these models facilitate modeling phenomenon such as preferential flow paths and fluid channelization commonly observed in fractured and faulted reservoirs.

3. Increase in fracture permeability due to slip

Several studies have shown that the fracture permeability increases with shear displacement across a fracture. The increase may either be due to mismatch produced by shear displacement between the fracture surfaces (Willis-Richards, 1995) or due to brecciation produced by the grinding between the adjacent rough fracture surfaces under high lithostatic stresses (Dholakia et al. 1998). This leads to the critically stressed fault hypothesis according to which fractures or faults that are mechanically alive are hydraulically alive and those mechanically dead are hydraulically dead (Barton et al., 1995). This means that faults with a ratio of shear to normal traction greater than the coefficient of sliding friction (normally about 0.6, Byerlee, 1978) would be expected to be permeable.

In the context of hydraulic stimulation, water from the hydraulic fractures diffuses into the surrounding natural fractures and faults reducing the effective normal stress resolved on the fractures, inducing shear slip (shear displacement), leading to enhancement in fracture permeability. Therefore, we can claim that pre-existing natural fractures and faults that are not mechanically active in the current stress state may not be permeable under ambient in-situ conditions, but they start permeating when slip is induced during stimulation. As pointed out by Das and Zoback (2013a), at high pore pressures induced by pressure diffusion during hydraulic fracturing, even poorly oriented (mechanically dead) faults are induced to slip. In section 5, we show how the newly-permeating fractures evolve the percolation zone and further enhance flow.

4. Effect of slip on the surrounding rock matrix

In this section, we utilize dynamic rupture theory to model the effect of seismic slip on small natural faults during hydraulic stimulation on the surrounding rock matrix. The aim is to investigate if there is any significant impact of dynamic slip on the surrounding rock permeability. We expect that as the rupture propagates on the fault, stress concentrations associated with the propagating rupture create inelastic shear and dilatant deformations around the fault leading to an increase in matrix porosity and permeability. The spatial extent of inelastic deformations from the fault surface and the magnitude of plastic strains produced are used to assess whether or not co-seismic slip on fractures/faults significantly increases rock permeability. Principles of dynamic rupture propagation are used to numerically model these volumetric strains and damage created along the fault plane (the methodology adopted is similar to the one discussed in Johri et al (2013), except that the model scale in that study is on the order of kilometers, while the scale in this study is on the order of 1-3 meters). Rupture propagation is studied using two-dimensional plain-strain models. The off-fault material is described by a Drucker-Prager elastic-plastic rheology. A similar assumption has also been made in other published studies on dynamic rupture propagation (Templeton and Rice, 2008; Johri et al. 2013). The coefficient of friction obeys a rate-and-state law that features the direct effect and evolution (over slip L which evolves over a characteristic distance R_0) towards a strongly velocity-weakening steady state friction coefficient. A complete description of the friction law and plasticity formulation is provided in Dunham et al., (2011a). The model parameters chosen to describe the friction law and the off-fault material rheology can be found in Johri (2012).

4.1 Model Development and Initial Conditions

A 1 meter long fault buried in a homogeneous half space is considered (Figure 1). This length is larger than the critical nucleation length (minimum fault length required for a rupture to nucleate), which is approximately 0.1 meters, but small enough to host microearthquakes of the order of magnitudes observed in microseismicity monitoring programs (magnitudes -1 to -3). The fracture is located at a depth of 8500 feet (2590 meters). A range of fault orientations with respect to the in-situ stress state is considered. An absorbing boundary condition is applied to

all the four sides of the model domain. The fault is assumed to be oriented along the X axis with the origin lying at the center of the fault. For the purpose of modeling, it is assumed that the fluid from the hydraulic fracture seeps into the surrounding formation and enters the fault from the left tip. The pore pressure, therefore, starts building up gradually around the left tip and induces slip on the fault when the effective normal stress has been sufficiently reduced over some critical rupture nucleation region. Thereafter, the slip nucleates towards the left tip of the fault and propagates along the positive X direction.

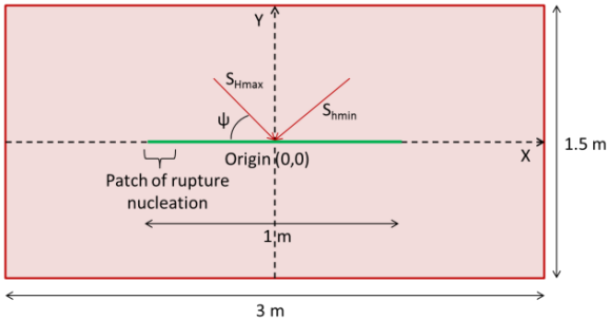

Figure 1: Two-dimensional idealization to model slip on a vertically dipping buried natural fault. The green line represents the fault surface.

4.2 Background stresses

Next, the model described above is evaluated for a normal faulting stress state. The vertical stress and the minimum horizontal stress are assumed to be the maximum and minimum principal stresses, while the maximum horizontal stress lies in the plane of the fault. The regional stress state was constrained by frictional strength using information on wellbore breakouts and drilling induced tensile fractures identified in image logs, and rock strength and coefficient of internal friction obtained from triaxial experiments (Sone, 2012). The vertical stress is obtained by integrating the density log which is 1.1 psi/ft. The minimum horizontal stress obtained from the measured fracture gradient is 0.65 psi/ft while the constrained value of maximum horizontal stress is 0.73 psi/ft. The fault is assumed to be located at a depth of 2.2 km. This results in the maximum (S_v), intermediate (S_{Hmax}) and minimum (S_{hmin}) principal stresses being 54.78 MPa, 36 MPa and 28.2 MPa respectively. Pore pressure is approximately hydrostatic (0.45 psi/ft – Sone and Zoback, 2012). We have considered 4 cases where the angle ψ between the fracture plane and the direction of the maximum principal stress (vertical direction) is 10˚, 20˚, 30˚ and 40˚. The value of the ratio of shear to normal stress τ/σ_n for the four cases is 0.43, 0.67, 0.70 and 0.63. Further simulation details and a discussion on the failure criterion is provided in Johri (2013).

4.3 Results

Figure 2a shows the profiles of the slip induced on the fracture at every 0.4 micro seconds for the case when the angle ψ between the fracture surface and the direction of the maximum horizontal stress is 30º. The maximum slip is approximately 0.15 mm. Assuming a square 1 m × 1 m fault, the scalar seismic moment is approximately

$M_0 = \mu Ad = (30 \times 10^9) N/m^2 \times 1m^2 \times 0.00015m = 45 \times 10^6$ Nm

where μ is the shear modulus (~ 30 GPa), A is the area of cross-section of the fault and d is the average slip. The magnitude of this micro earthquake is $M_w = (2/3 \log M_0 - 6.03) = -0.97 \approx -1$

This would be one of the larger magnitude earthquakes since most of the micro-earthquakes recorded are approximately -2 to -3 in magnitude.

Figures 2 (b)-(e) shows the plastic strain field generated due to slip induced on faults which are oriented such that the angle ψ between the fracture and the direction of maximum principal stress (vertical direction) is 10˚, 20˚, 30˚ and 40˚ (the fault planes have been rotated to be horizontal to facilitate representation). In these simulations, the rock is assumed to be cohesion-less. We neglect cohesion as we assume that the deformation processes prior to and during initial fault formation would have intrinsically damaged the surrounding rock leading to near-negligible cohesion values. In Figures 2 (b)-(e), we notice that the distribution of plastic strains are in accordance with Templeton and Rice (2008), who have shown that the region undergoing inelastic deformation around a propagating crack tip depends on the angle ψ between the fault plane and the direction of maximum principal stress. For ψ less than 20º, the inelastic deformation occurs primarily in the compressional quadrants while for ψ larger than 45º, the inelastic deformation occurs exclusively in the extensional quadrants. In Figure 2b where ψ is 10º, plastic strains are

primarily restricted to the compressional quadrant (with respect to the direction of rupture propagation), and the plastic strain lobe transitions to the extensional quadrant as angle ψ increases (Figures 2c and 2d) until it is completely in the extensional quadrant when ψ is 40º (Figure 2e). We also observe that the spatial region experiencing plastic strains is larger for larger values of ψ.

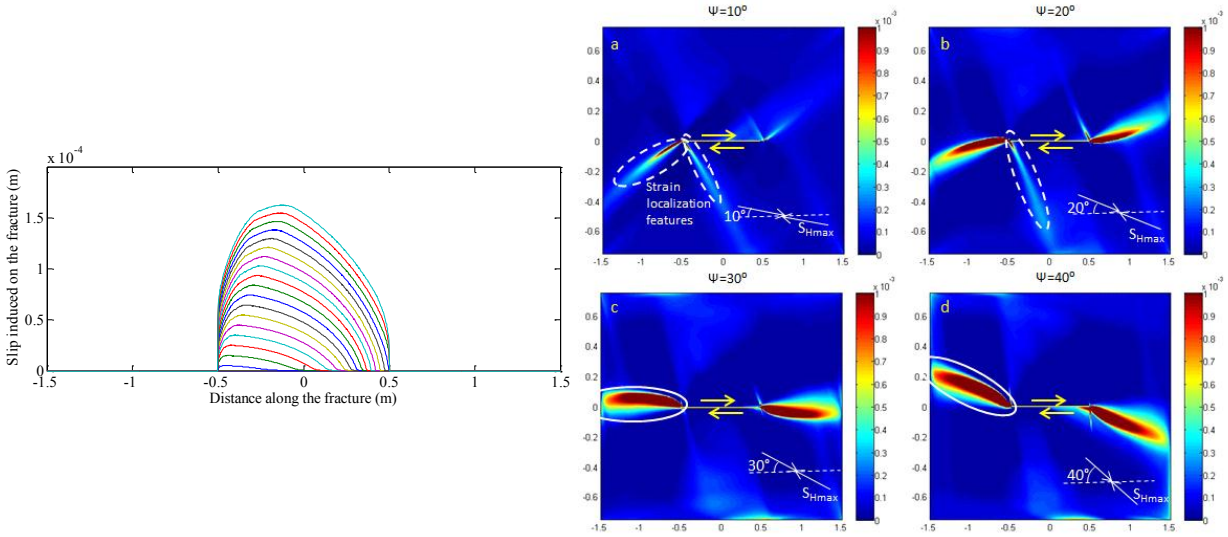

Figure 2: (a) Plot showing the profile of slip induced on a natural fracture during hydraulic fracturing. Various lines represent slip profile at every 0.4 micro-seconds of rupture propagation on the fault. (b) – (e) Equivalent plastic shear strain field generated due to slip induced on a 1 m long fault. All dimensions are in meters. The angle ψ between the fracture plane and the vertical stress is (b) 10º (c) 20º (d) 30º (e) 40º. The colors represent plastic dilatant strains. Strain localization features suggestive of the creation of new fractures in (b) and (c) are shown by white dotted ellipses. Regions of concentrated extensional plastic strains (shown by solid white ellipses) in (c), (d) and (e) further extend the effective permeable length of fractures.

We notice from Figures 2 (b)-(e) that the area undergoing inelastic deformations is very limited and the magnitude of plastic strains induced is modest the maximum plastic strain being approximately 0.001. Performing a simple volume balance, if we consider a volume V having porosity ∅, the volume created by dilatant plastic strain within this element of volume V is $\beta\gamma^p V$ where β is the dilatancy and γ^p is the shear plastic strain. The new porosity, therefore, is approximately $\frac{\emptyset V+\beta\gamma^p V}{V+\beta\gamma^p V} = \frac{\emptyset+\beta\gamma^p}{1+\beta\gamma^p} \sim (\emptyset + \beta\gamma^p)$. Assuming a dilatancy of 0.28 and maximum shear plastic strain of 0.001, the increase in porosity is 0.00028. This is a negligible increase in the 0.02-0.09 porosity of shale, and probably has a negligible impact on permeability. However, we notice from Figures 2b and 2c the formation of strain localization features at the tips of the slipping fault. These are suggestive of the formation of new fractures. The size of fractures formed is very similar to (same order of magnitude) the size of the slipping fault. We also notice concentrations of dilatant plastic strains at the ends of the slipping fault in Figures 2d and 2e. This is suggestive of an increase in the effective permeable length of the fracture or regions of enhanced permeability which may contribute towards the enhancement of the hydraulically connected fracture network. The implications of the formation of new fractures and increase in the effective permeable length of slipping fractures are discussed in section 5.

5. Formation of new fractures and increase in the percolation zone

Although slip on small natural faults does not significantly affect the porosity and permeability of the surrounding rock matrix, modeling in the previous section suggests that it leads to an increase in the effective permeable length of the slipping fractures, and the creation of new fractures. Although strain localization features are only noticed when we ignore rock cohesion, a case could be made that the rock strength measured on core samples is not representative of the entire rock mass in the vicinity of the existing faults. Figure 2b suggests that two fractures form at approximately 30˚ and 120˚ with respect to the plane of the slipping fault (in the compressional quadrant) when ψ is 10˚ while Figure 2c suggests the formation of one fracture at an angle of 120˚ from the fault tip in the compressional quadrant when ψ is 20˚. The relatively thicker lobes of extensional plastic strains at the tips of the slipping fault (Figures 2c, 2d and 2e) are suggestive of an increase in the effective permeable length of the fault by approximately two times the original fault length. The formation of new fractures and increase in the effective

length of slipping fractures can potentially increase the fracture network connectivity within the reservoir and hence the percolation zone. Since the flow rate depends on the total surface area of fractures through which flow can occur, i.e. the total area of fractures hydraulically connected (via a continuous network of hydraulically active fractures) to the well, an increase in percolation zone translates into an increase in flow rates. ($Q = \alpha\sqrt{t}$ where Q is the cumulative production to time t, and $\alpha = A\left(\frac{P_r^2 - P_{bhf}^2}{P_s}\right)\sqrt{\frac{\phi_m K_m c_f}{\pi\eta}}$ where A is the percolation zone, P_r, P_{bhf}, and P_s are the reservoir pressure, bottom hole flowing pressure and surface pressure respectively, and ϕ_m, K_m, c_f, and η are the matrix porosity, matrix permeability, gas compressibility and gas viscosity.

The matrix permeability of Barnett is on the order of ~ 100 nd (Vermylen and Zoback, 2012). Therefore, it is almost certain that most of the gas flow occurs through fractures. We hypothesize, however, that most flow in the Barnett, in fact, occurs only through the mechanically active fractures that have slipped due to shear and the hydraulic fractures. Obviously, it is only those critically stressed fractures that are hydraulically connected to the producing well that contribute to fluid flow. During hydraulic stimulation, pore pressures in the pre-existing fractures in the percolation zone can reach values approaching the minimum principal stress. Such highly elevated pore pressures cause several natural fractures and faults in the surrounding formation to slip, enhancing their permeabilities in the process (Das and Zoback, 2012 b). Induced slip not only increases the population of the critically stressed faults (and hence the percolation zone), but it may also create new fractures (as shown in the previous section) that increase the fracture connectivity within the reservoir. We show this increase in the percolation zone by modeling a fracture network in the following section.

5.1 Model development

We investigate fracture connectivity and increase in the percolation zone as a result of hydraulic stimulation in the framework of discrete fracture networks (DFNs). The FracMan software package is used for modeling the DFN. The area of study is the Barnett reservoir. A 1200 ft × 600 ft × 2250 ft reservoir domain (along a 2250 ft long segment of a horizontal well that was perforated and fractured) is modeled (Figure 5a). Hydraulic fractures are modeled as hexagonal planes with an effective radius of 200 feet (effective radius of a polygon is defined as the radius of a circle whose area is equal to the area of the polygon). The spacing between hydraulic fractures created is assumed to be ~ 300 feet.

5.2 Generation of the Discrete Fracture Network

Background fractures in the model domain are stochastically generated using the FracMan software suite (FracMan manual, 2011). The parameters required for stochastic generation of fractures are the fracture density, distribution of fracture orientations, and distribution of fracture sizes. Fracture density in various intervals of the reservoir is derived from image logs. Figure 3a shows the schematic of the strike of fractures identified in the image log and intersecting the well while Figure 3b shows the cumulative density plot of fractures identified in the wellbore image log. The slope of the cumulative density plot is representative of the fracture density (P10 - number of fractures per unit length). Five regions of varying P10 (marked intervals a-e) along the well can be identified. Fracture density in intervals a-e are 0.5, 0.0025, 0.039, 0.13 and 0.28 fractures/m respectively.

Next, statistical analysis is performed to identify various fracture sets in the fracture data obtained from the image log using the ISIS (Interactive Set Identification System) feature of FracMan. ISIS defines fracture sets from field data using an adaptive probabilistic pattern recognition algorithm. The distribution of the orientations of fractures assigned to each set is calculated, and then fractures are reassigned to sets according to probabilistic weights proportional to their similarity to other fractures in that set. The orientations of the fracture sets are then recalculated and this process is repeated until the fracture set assignment is optimized. Essentially, the statistical properties of each set are derived from the statistical properties of the fractures assigned to that set, and then fractures with a low probability of belonging to that set are removed and reassigned to another set. This ensures that the fractures are divided into groups being geologically and hydrologically similar. A complete description of the theory behind the pattern recognition algorithm can be found in the FracMan manual (2011). Figure 3c shows the contoured stereoplots of the major fracture sets present in the fracture population. There appear to be two major fracture sets. A Fisher distribution is assumed to describe the distribution of fracture orientations in the two sets. The mean orientation of poles in the first fracture set is approximately a trend of 10° and a plunge of 4° with a dispersion of 50,

while that in the second fracture set is a trend of 320°, plunge of 8° with a dispersion of 20. The larger the dispersion, the more concentrated are the fracture orientations about the mean orientation. 75% of the total fracture population belongs to the first set while 25% belong to the second set.

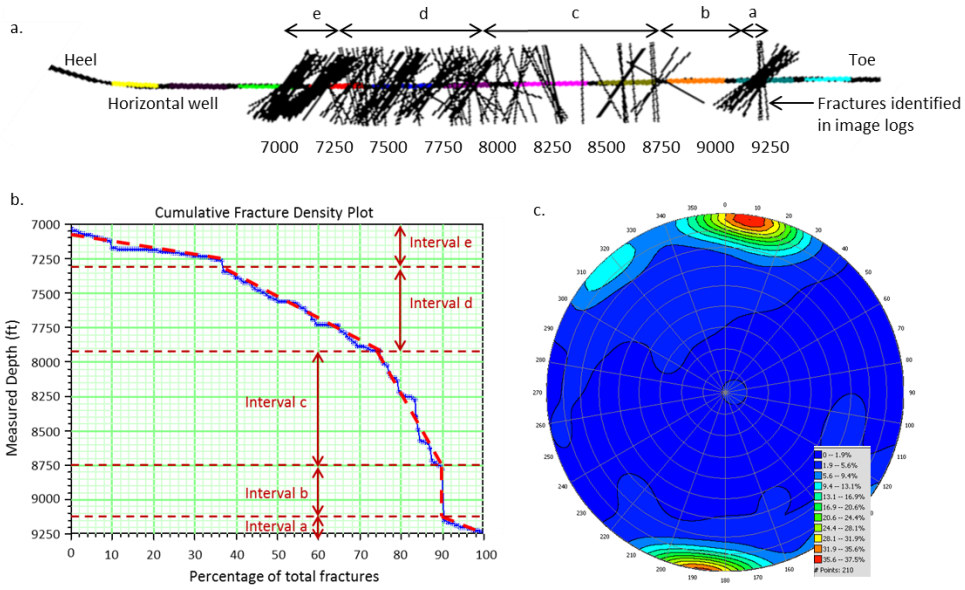

Figure 3: (a) Schematic of the well along with fractures identified in the image log and intervals of varying fracture density. Dimensions are in feet (b) Cumulative fracture density plot of fractures identified in the image log. Slope of the line represents the fracture density. The five intervals represent regions having distinctly different fracture densities. (c) Contoured stereonet of the fracture poles

The next step is to assign a size and shape to these fractures. It is largely believed that power law models describe the length distribution of fractures. A large number of studies have been devoted to analyzing length distribution of fractures (Odling, 1999) in order to test the power law scaling model. However, despite numerous analyses and efforts, the statistical relevance of power law models is not established amongst the scientific community, primarily due to difficulties in obtaining a robust statistical analysis on severely limited data sets. However, Odling et al. (1999) have reported that the fracture lengths appear to follow a power law distribution ($N(l) = L_{min} l^{-n}$) with a decay rate n of ~2.1 over up to 4-5 orders of magnitude. In this study, we assume that fracture lengths honor such a power law distribution and constrain the minimum fracture length L_{min} to be 4 feet. The distribution of fracture lengths is shown in Figure 4a.

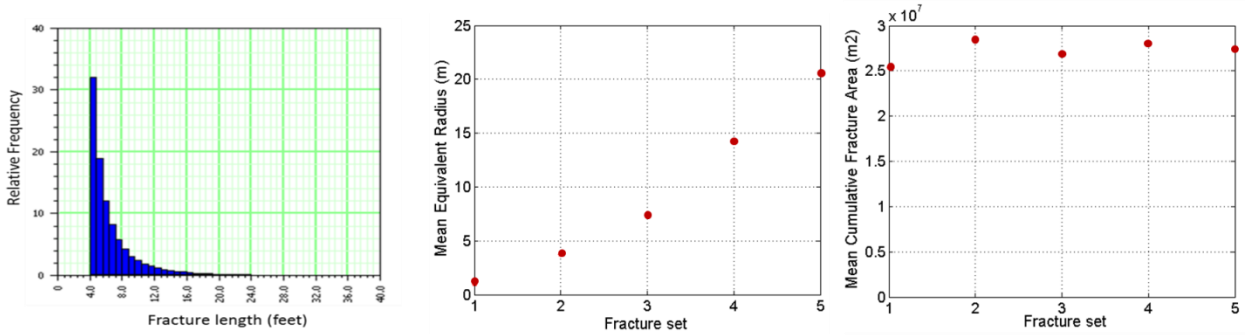

Figure 4: (a) Histogram of length of fractures assuming a power law distribution. Minimum fracture length (constrained) is 4 feet. (b) Mean equivalent radius of the 5 fracture sets considered. (c) The total fracture area of the 5 fracture sets. The 2 plots show that although we consider fracture sets with significantly different mean fracture sizes, the total fracture area for attaining a certain target fracture density measured along a well is almost identical.

Since the choice of L_{min} impacts the average fracture size and may seem to have implications on the overall analysis, we show that our analysis is independent of this assumption with the help of a statistical experiment. We consider 5 different length distributions (each following a power law $L = L_{min} l^{-n}$, but with a different value of L_{min}). The smaller the chosen L_{min}, the smaller will be the mean fracture length. We generate multiple realizations

with each of the above 5 distributions and average them (for statistical robustness) in order to obtain the mean fracture size and mean cumulative fracture area in each of the 5 cases. Figure 4b shows the average fracture size for the 5 cases of varying length distributions while Figure 4c shows the mean cumulative fracture area for the 5 cases. We observe that although we are considering remarkably different fracture sizes, the total fracture area essentially remains the same. It basically means that in order to obtain a certain target fracture density along a well, a larger number of smaller fractures are required to obtain a certain target fracture density as compared to larger fractures. However, the total fracture area is almost invariant. Since the flow rate depends on the percolation zone, which is only a measure of the total fracture area, our analysis should be independent of the fracture length distribution. In the absence of constraints on the aspect ratio of fractures, we assume fractures to be square-shaped in this study. The geometrical properties of background fractures and those comprising the damage zones are hence fixed. Once the fracture intensity, size, and orientation distribution parameters in each interval are obtained, these intervals are stochastically populated with fractures belonging to the sets present in that interval until the target fracture density P10 along the section of the well is reached.

5.3 Fracture connectivity analysis and percolation zone

Figure 5b shows the DFN model comprising all fractures present in the model domain. None of the fractures are critically stressed (or mechanically active) in the present day stress state (under in situ hydrostatic pore pressure conditions) leading to an almost impermeable fracture population, and negligible percolation zone and flow rates. Hydraulic stimulation creates hydraulic fractures and pressurizes the formation leading to an increase in pore pressure. Elevated pore pressures can measure up to 0.9 times the minimum principal stress. As a result, several natural fractures slip leading to increase in fracture permeability. This dramatically increases the network of hydraulically conductive (critically stressed) fractures that is hydraulically connected to the well (percolation zone) (Figure 5c). Modeling slip across natural faults (section 4) suggests the formation of new fractures around poorly oriented faults and an increase in the effective permeating length of the slipping faults. We identify the poorly oriented faults and fractures ($5° < \psi < 25° - 25$) in the percolation zone, and introduce new fractures at their tips (two fractures when ψ lies between 5° and 15°, and one fracture when ψ lies between 15° and 25°, as mentioned in section 4). We also increase the effective permeating length of the slipping fractures. Figure 5d shows the network of new fractures. The new critically stressed fractures not only contribute to flow themselves, but also increase the connectivity of the pre-existing fracture network, thereby increasing the percolation zone. Figure 5e shows the updated percolation zone, i.e. the new population of critically-stressed fractures and faults that are hydraulically connected to the producing well (comprising of both the pre-existing and newly formed fractures). The significant increase in percolation zone leads to significantly larger flow rates.

There are three factors that enhance the percolation zone. First is the contribution from the area created by the main hydraulic fractures themselves. Second is the set of pre-existing fractures and faults that are activated as a consequence of increase in pore pressure, and are also hydraulically connected to the well. The third contributor is the set of new critically stressed fractures hydraulically connected to the well, i.e. the newly percolating fractures. In the model described above, contribution from the hydraulic fractures is 8.79×10^5 sq. ft. Percolation zone obtained by considering the hydraulic fractures and pre-existing critically stressed fractures and faults is 8.38×10^7 sq. ft (Figure 5c – increase of ~ 95 times), while the percolation zone obtained by considering the total fracture population, including those newly created due to slip on pre-existing faults is 15.47×10^7 sq. ft (Figure 5e - ~176 times increase). Clearly, the contribution from the surface area of the hydraulic fractures is insignificant compared to contributions from the hydraulically connected fractures and faults in enhancing the percolation zone, and hence the flow rates. This suggests that stimulating the pre-existing fracture network, and not the creation of hydraulic fractures is key to stimulation. The relevant statistics, i.e. number of all and critically stressed fractures along with the percolation zone before and after reservoir stimulation can be found in Johri (2012).

We also consider a case with a larger number of hydraulic fractures, assuming the inter spacing between hydraulic fractures to be 50 feet (as opposed to 300 feet earlier). Figure 6a shows the model domain with 45 hydraulic fractures with a spacing of 50 feet. By considering a larger number of hydraulic fractures, we expect greater fracture connectivity, and hence a larger percolation zone. Figure 6b shows the percolation zone considering only the pre-existing fractures while Figure 6c shows the percolation zone considering both, the pre-existing fracture population and the newly formed fractures. The percolation zones in Figures 6b and 6c are 9.08×10^7 sq. ft. and 16.07×10^7 sq. ft. respectively, while the contribution from the area of the hydraulic fractures alone is only 5.66×10^6 sq. ft.

Clearly, the contribution from natural fractures and faults is significantly larger than that from hydraulic fractures alone. The relevant statistics, i.e. number of all and critically stressed fractures along with the percolation zone before and after reservoir stimulation are provided in Johri (2012).

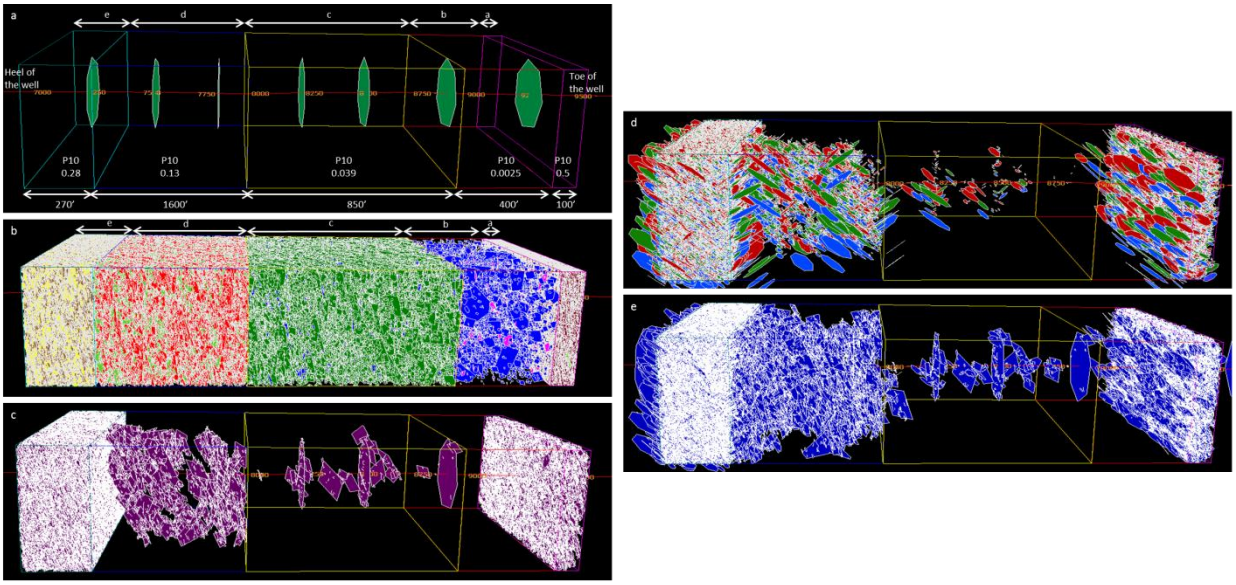

Figure 5: (a) Model domain showing the modeled portion of the reservoir along a 2250 feet long segment of a horizontal well. The green surfaces represent the created hydraulic fractures. The five regions (numbered a-e) outlined in different colors represent regions of different P10 (fracture density per unit distance) observed in image logs. The red line represents the well trajectory. All dimensions are in feet (b) DFN showing the pre-existing fracture population. Various colors represent fractures belonging to two different sets in each of the five intervals (c) Critically-stressed fracture network hydraulically connected to the well i.e. percolation zone post stimulation considering only the initial fracture population (d) New fractures created due to slip induced on poorly-oriented fractures (e) Critically-stressed fracture network hydraulically connected to the well i.e. percolation zone post stimulation considering both, the preexisting and newly formed fractures.

Figure 6d shows the contributions towards the percolation zone from the three contributors previously discussed, for both, an inter hydraulic-fracture spacing of 300 feet (in blue) and 50 feet (in red). Clearly, the contribution from natural fractures and faults is significantly larger than that from hydraulic fractures alone. It is also clear that although the percolation zone obtained with a larger number of hydraulic fractures is larger than that obtained with fewer hydraulic fractures, the difference is subtle (~3-8 %), most of that difference being due to a larger area of hydraulic fractures created and not due to the difference in the activated percolation zone. This clearly suggests that it is not the number of hydraulic fractures, but the pre-existing fracture network that determines the potential of the reservoir to be stimulated. If the formation is poorly fractured, the creation of a hydraulic fracture will activate very few fractures, in which case the percolation zone will primarily comprise of the area of hydraulic fractures created. We can, therefore, hypothesize that for a successful stimulation program, the pre-existing fracture density should be larger than a critical/threshold value such that they can be efficiently stimulated during fracturing operations in order to create a pervasive, hydraulically connected fracture network that penetrates deep into the formation, maximizing the contact area of the hydraulically connected fracture network with the reservoir, and hence the percolation zone.

Next, we discuss the variability in stimulation during various stages of hydraulic fracturing, considering the case with an inter-hydraulic spacing of 300 feet. The bar chart in Figure 7 shows the percolation zone created during various stages of hydraulic fracturing (we assume that each of the seven hydraulic fractures constitute a different stage, assuming one perforation per stage), along with the contributions to the total percolation zone by the hydraulic fractures, pre-existing percolating fractures and the newly-created percolating fractures. To ease visualization of relative contributions, Figure 7a shows the percolation zone on a logarithmic scale while Figure 7b shows the percolation zone on a linear scale. It is clearly seen that the relative contribution from hydraulic fractures is almost negligible (Figure 7a). Contributions from pre-existing and newly formed percolating fractures seem to be on the same order of magnitude (Figure 7b). Figure 7c shows the percolating zone associated with each of the stages, each stage represented by a different color. Stage 7 (close to the heel of the horizontal well) appears to be the most

prolific stage with maximum stimulation followed by stage 1 (close to the well toe). Stages 5 and 6 produce moderate reservoir stimulation, while stages 2, 3 and 4 result in insignificant stimulation. This is due to the scarce population of natural fractures in the vicinity of these stages to start with, suggesting that a substantial fracture population is critical to stimulating a reservoir. Regions with a larger population appear to have a higher potential for stimulation. The above analysis, therefore, suggests that maximum flow rates would be observed after stage 7, followed by stages 1, 5 and 6. Stages 2, 3, and 4 would have minimal flow rates. This, therefore, explains the variability in the effectiveness of reservoir stimulation, and hence production in different regions of the reservoir.

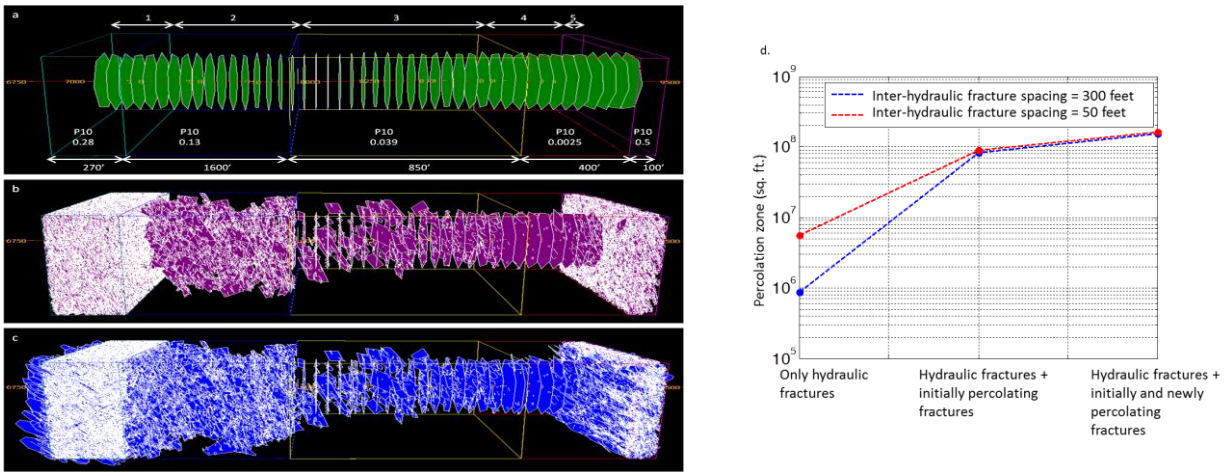

Figure 6: (a) Model set-up showing the various intervals of varying fracture density, horizontal well and hydraulic fractures with an interspacing of 50 feet (b) Critically-stressed fracture network hydraulically connected to the well i.e. percolation zone post stimulation considering only the initial fracture population (c) Critically-stressed fracture network hydraulically connected to the well i.e. percolation zone post stimulation considering both, the preexisting and newly formed fractures (d) Contributions from the three primary contributors – hydraulic fractures, pre-existing percolating fractures and newly created percolating fractures, towards the percolation zone. Red line represents the case when the hydraulic fracture spacing is 50 feet while blue line represents the case when the inter-spacing between hydraulic fractures is ~ 300 feet.

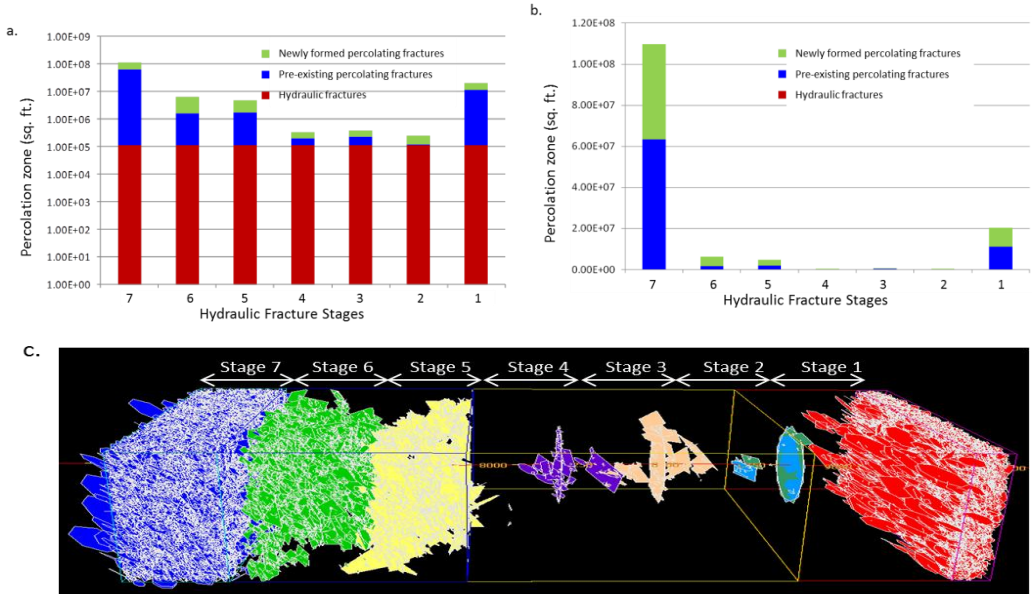

Figure 7: Percolation zone resulting from various stages of hydraulic fracturing performed along a horizontal well, along with relative contributions from the hydraulic fracture, pre-existing percolating fractures, and newly formed percolating fractures. Percolation zone shown on a (a) logarithmic and (b) linear scale (c) Fracture network comprising the percolation zone associated with various stages.

6. Conclusions

This study shows that co-seismic slip induced on natural fractures and faults as a result of increase in pore pressure during hydraulic fracture operations does not produce significant plastic strains that could potentially create porosity and enhance the matrix permeability of the rock surrounding the faults. However, such slip increases fracture permeability. Besides, slip on faults leads to the formation of fractures at the fault tips and an increase in the effective permeable length of the fault. This increases the percolation zone and reservoir penetration not only by enhancing the cumulative fracture surface area but also increasing the connectivity of the pre-existing fracture network. Increase in the percolation zone appears to depend more critically on the characteristics of the initial fracture population than the number of hydraulic fractures created. Areas where the initial fracture density is low do not experience a large increase in percolation zone after stimulation even if the formation is severely hydraulically fractured, suggesting that reservoir stimulation is directly correlated to the initial fracture population. This could explain the great variability in the productivity of shale gas wells, and reservoir stimulation response in a given area. Therefore, reservoir fracture characterization along with prediction of the pre-existing fracture network and the regional stress state could help predict the effectiveness and spatial variability of reservoir stimulation, and help improve the efficiency of hydraulic fracturing operations. If this is true, shale gas development could be approached from a predictive perspective by developing modeling techniques that facilitate reservoir fracture characterization (representative fracture size, intensity and orientation distributions), an understanding of the stress state and its impact on reservoir stimulation, along with predicting stimulation pressures required to optimize reservoir stimulation.

7. Acknowledgements

This work was funded by the Stanford Rock Physics and Borehole Geophysics Research Consortium. FracMan software was provided by Golder Associates and GMI-Imager was provided by Baker Hughes. Numerical simulations were conducted at the Stanford Center for Computational Earth and Environmental Science (CEES).

8. References

Barton C. A., M. D. Zoback, and D. Moos. 1995. Fluid flow along potentially active faults in crystalline rock. Geology, 23, 683-686. doi: 10.1130/0091-7613(1995)023<0683:FFAPAF>2.3.CO;2

Das, I., and Zoback, M. D. (2013a). Long-period, Long-duration Seismic Events During Hydraulic Fracturing Stimulation of Shale and Tight Gas Reservoirs Part 1: Waveform Characteristics, Geophysics (submitted).

Das, I., and Zoback, M. D. (2013b). Long-period, Long-duration Seismic Events During Hydraulic Fracturing Stimulation of Shale and Tight Gas Reservoirs Part 2: Location and Mechanisms, Geophysics (submitted).

Dholakia, S. K., Aydin, A., Pollard,D. D., and Zoback, M. D. (1998). Fault-controlled hydrocarbon Pathways in the Monterey formation, California. American Association of Petroleum Geologists Bulletin 82: 1551-1574

Dunham, E. M., Belanger, D., Cong, L., and Kozdon, J. E. (2011). Earthquake Ruptures with Strongly Rate-Weakening Friction and Off-Fault Plasticity, Part 1: Planar Faults. Bulletin of the Seismological Society of America, 101(5), 2296-2307. doi:10.1785/0120100075

Johri, M., Dunham, E. M., Zoback, M. D., and Fang, Z. (2013). Modeling fault damage zones using dynamic rupture propagation and comparison with field observations. Journal of Geophysical Research (submitted)

Johri, M. (2012). Fault damage zones - observations, dynamic modeling, and implications on fluid flow. Ph.D. thesis, Stanord University.

Odling, N. E., P. A. Gillespie, B. Bourgine, C. Castaing, J.P. Chiles, N. P. Christiansen, M. Eeles, E. Fillion, A. Genter, L. Madsen, C. Olsen, R. Trice, J. J. Walsh, and J. Watterson. 1999. Variations in fracture system geometry and their implications for fluid flow in fractured hydrocarbon reservoirs. Petroleum Geoscience, 5, 373-384. doi: 10.1144/petgeo.5.4.373

Sone, H., and Zoback, M. D. (2013). Mechanical Properties of Shale Gas Reservoir Rocks - Part 1: Static and Dynamic elastic properties, and anisotropy. Geophysics (submitted)

Templeton, E. L., and Rice, J. R. (2008). Off-fault plasticity and earthquake rupture dynamics: 1. Dry materials or neglect of fluid pressure changes. Journal of Geophysical Research, 113(B9), 1-19. doi:10.1029/2007JB005529

Vermylen J. P., and Zoback, M. D. (2011). Hydraulic fracturing, microseismic magnitudes, and stress evolution in the Barnett shale, Texas, USA. Society of Petroleum Engineers Annual Technical Conference, 140507.

Willis-Richards, J., Watanabe, K., and Takahashi, H. (1996). Progress toward a stochastic rock mechanics model of engineered geothermal systems. Journal of Geophysical Research, 101 (B8), 481-17, 496. doi: 10.1029/96JB00882

Zoback, M. D., Kohli, A., Das, I., and McClure, M. (2012). The Importance of Slow Slip on Faults During Hydraulic Fracturing Stimulation of Gas Shale Reservoirs. SPE-155476 Americas Unconventional Resources Conference, Pittsburg, Pennsylvania, USA, 5-7 June, 2012.